Development of an automated null ellipsometer for characterising large-aperture, high-reflectance optical coatings used in DiPOLE systems

Contact: danielle.clarke@stfc.ac.uk

D. L. Clarke
Central Laser Facility,
STFC Rutherford Appleton Laboratory,
Harwell Innovation Campus,
Oxfordshire, OX11 0QX

L. Dixon
Department of Physics,
University of Surrey,
Guildford, GU2 7XH

M. De Vido
Central Laser Facility,
STFC Rutherford Appleton Laboratory,
Harwell Innovation Campus,
Oxfordshire, OX11 0QX

M. J. D. Esser
Centre for Doctoral Training in Applied Photonics,
Heriot-Watt University,
Edinburgh, EH14 4AS

Abstract

Characterising the properties of high-reflectance, optical coatings for high-power laser systems is important for improving optical-to-optical efficiency and extending system capabilities. In particular, removing the phase delay introduced by these optical coatings is important for reducing a large cause of loss, in high-power laser systems, known as depolarisation. To remove phase delay, it must first be quantified. Null ellipsometry is a method for measuring phase delay, hence, a partially-automated, null ellipsometer has been commissioned to characterise coatings over a wide range of angles. Automation of the null ellipsometer has both reduced measurement time and increased accuracy.

1 Introduction

Laser systems that are able to amplify nanosecond pulses to high energies (multi-J) at high repetition rates (multi-Hz) are important for a wide range of industrial and scientific applications. These include: industrial material processing, such as laser shock peening [1], inertial confinement fusion technology [2] and research into the extreme states of matter found at the centre of extra-solar planets [3]. Characterisation of the optical components in high-power laser systems is a vital step for the development and optimisation of these systems. In particular, understanding the losses introduced by individual components in an optical system is essential for reducing unwanted effects. To date, two such high-power laser systems, known as DiPOLE (Diode Pumped Optical Laser for Experiments) laser systems, have achieved world-leading, average output powers exceeding 1 kW at a wavelength of 1030 nm by producing nanosecond pulses of energy in excess of 100 J at a repetition rate of 10 Hz [4][5]. Since commissioning, improvements and upgrades to the DiPOLE laser system has led to 150 J operation at 10 Hz [6]. Projects to further scale the DiPOLE technology behind these systems to higher average powers, by increasing both the energy per pulse and the pulse repetition rate, are currently underway [7].

In addition, methods to make DiPOLE systems suitable for a wider range of applications are also under investigation. For example, non-linear frequency conversion of the 1030 nm DiPOLE beam through second harmonic generation (SHG) to 515 nm [8] makes the system suitable for pumping Titanium-doped Sapphire (Ti:Sapphire), a common choice for the gain media of petawatt-class chirped pulse amplification (CPA) systems [9][10][11]. However, due to the nature of the frequency conversion process, optical-to-optical efficiency is dependent on the polarisation purity of the input beam. The introduction of different polarisation states across the aperture of a beam is an undesirable effect, called depolarisation, shown in Figure 1. Reduction of depolarisation in the DiPOLE 1030 nm beam will minimise losses during SHG allowing for higher average output powers at 515 nm. Optimising SHG is a particularly important task for the new CPA 10 Hz petawatt, Ti:Sapphire-based EPAC laser system, under development at the Central Laser Facility in Oxfordshire [12].

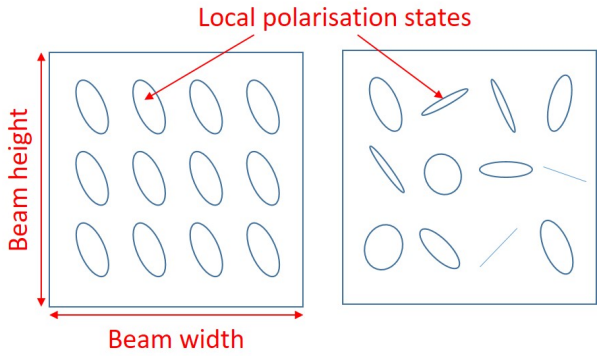

Figure 1: Cross section diagram of a uniformly polarised beam (left) compared with a depolarised beam (right).

DiPOLE systems are based on a multi-pass geometry where the beam passes through the amplifier head,

shown in Figure 2, multiple times. The main source of depolarisation in DiPOLE systems arises in the amplifier head [13]. The interplay between the thermal load, from the laser pump sources, and cooling, from the cryogenic Helium gas, gives rise to large thermal gradients across the gain medium. Figure 2 shows how the gain media slabs and amplifier head optics are subject to simultaneous heating and cooling processes. Parts of the slab at higher temperatures expand more than those at lower temperatures, creating non-uniform stresses. When optical components are stressed, they exhibit stress-induced birefringence. This causes the material to behave like a non-uniform retardation element that changes the polarisation of the beam across the beam aperture, or depolarises the beam.

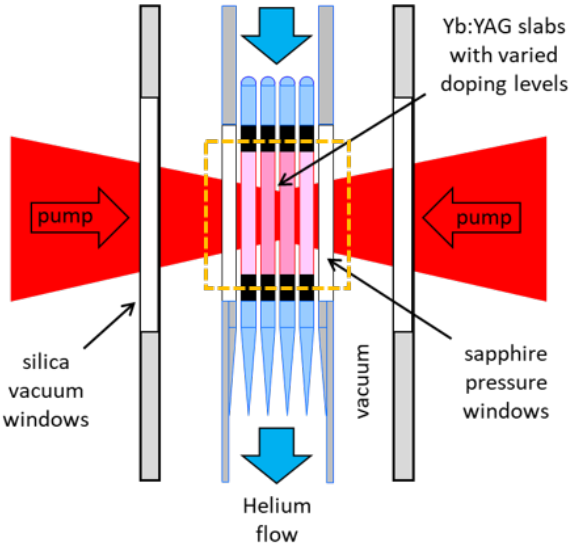

Figure 2: Cross-section of the DiPOLE amplifier head. The area enclosed by the yellow dotted lines shows the optics, in particular the gain medium and pressure windows, that are subject to simultaneous heating and cooling, resulting in stress-induced birefringence.

While there are several depolarisation compensation methods described in the literature for reducing depolarisation [14][15], they are ineffective in DiPOLE systems. The cause of this is believed to be a phase delay (change in phase between s- and p- polarisation components) introduced by large-aperture, high-reflectance coatings on mirrors in the multi-pass. Figure 3 shows how the phase delay of these coatings is predicted to behave for different angles of incidence for a wavelength of 1030 nm. Phase delay renders known depolarisation compensation methods ineffective. Therefore, methods to quantify, and potentially remove the effects of, phase delay is required for efficient 515 nm DiPOLE systems to be realised.

One solution is to develop high-reflectance coatings that do not introduce phase delay while maintaining the required levels of high reflectance, low scatter and

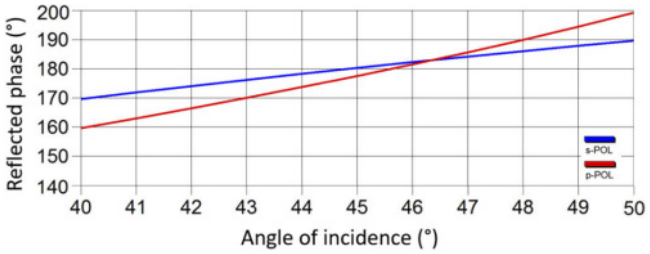

Figure 3: Theoretical phase delay introduced upon reflection off a DiPOLE high-reflectance coating, optimised for reflection at 45°, over a range of incident angles at a wavelength of 1030 nm (courtesy of Manx Precision Optics).

high damage threshold. An automated optical setup, based on a null ellipsometer [16], has been developed to measure phase delay (Section 4.1). Collaboration with coating supplier Manx Precision Optics to develop high-reflectance coatings with zero phase delay at the operational incidence angle is in progress. This report details the experimental setup, control software and calibration of the null ellipsometer as well as results showing the phase delay introduced by these coatings and future developments for improving measurement accuracy.

2 Background

2.1 Methods of Null Ellipsometry

The null ellipsometer is a simple setup consisting of a light source (source), a linear polariser (polariser), a QWP (compensator), the test piece (sample), another linear polariser (analyser) and a power meter (detector). This particular arrangement of the null ellipsometer is known as the polariser-compensator-sample-analyser, or PCSA, arrangement, seen in Figure 4. Components in the input arm produce a beam with a known polarisation state and the detection arm is designed to measure how much the polarisation changes from this known state, upon reflection off the test sample.

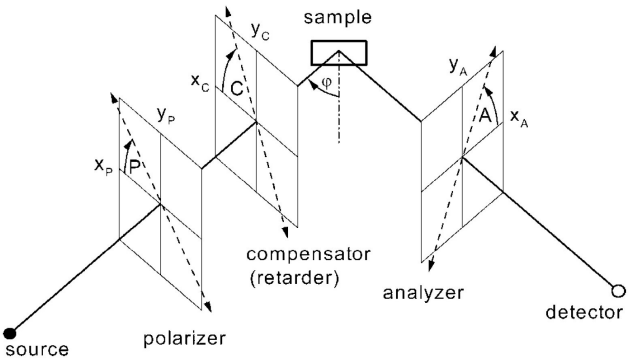

Figure 4: A single-wavelength, null ellipsometer in the PCSA arrangement [16].

The plane of incidence is the plane a beam parallel to the table makes when reflected off the sample. The face of the sample, or sample plane, should be perpendicular to the plane of incidence. The angle, in degrees, of the polariser, P, compensator, C, and analyser, A, are always measured anti-clockwise from the plane of incidence when looking into the beam.

The technique of manipulating P, C and A to achieve a null signal on the detector is discussed in Section 2.2. It is at this null condition that P, C and A can be used to calculate the ellipsometric parameters: phase delay, Δ, and amplitude ratio, Ψ. These parameters are related by the Fresnel reflectance ratio, ρ, given in Equation 1, where r_s and r_p are the amplitude reflectivities and δ_s and δ_p, are the phases of the s- and p-polarisations of light, respectively. The ellipsometric parameters can be used to calculate quantities such as film thickness and refractive index of coatings [17][18], however, only phase delay is of interest here.

$$\rho = tan(\Psi)\ e^{i\Delta} = \frac{r_p}{r_s} e^{i(\delta_p - \delta_s)} \tag{1}$$

2.2 Nulling Scheme

In null ellipsometry, a common method of finding a null condition is by setting C = $\pm$ 45° and iteratively rotating the polariser and analyser until a null is observed on the detector. Due to the 180° periodicity of linear polarisers and QWPs, there are 32 possible P, C and A combinations that produce a null, however, only four independent combinations are of interest. The four nulls are separated into four different zones numbered 2 and 4, when C = + 45°, and numbered 1 and 3, when C = - 45°. While one set of P, C and A values in a single zone can be used to calculate phase delay, shown in Table 1, measurements in all four zones, or four-zone measurements, are preferred. This is because errors introduced by component imperfections and angle misalignments with the plane of incidence on the polariser, compensator and analyser cancel out.

Zone	C	Δ	Ψ
1	- $\frac{\pi}{4}$	$2P_1 + \pi/2$	A_1
2	+ $\frac{\pi}{4}$	- $2P_2$ - $\pi/2$	A_2
3	- $\frac{\pi}{4}$	$2P_3$ - $\pi/2$	- A_3
4	+ $\frac{\pi}{4}$	- $2P_4$ + $\pi/2$	- A_4

Table 1: Relationship between the angles of the polariser, P, compensator, C, and analyser, A, with phase delay, Δ, and phase amplitude, Ψ.

To find the nulls in zones 2 and 4, set C = + 45°, iteratively rotate P and A between 0° and 180°, until a minimum is observed on the detector, and record P and A values. Leave C = + 45°, rotate the polariser by 90° and move the analyser to 180° - A. Make small iterative adjustments until minimum signal is achieved and record P and A values. P and A values between 0° and 180° are required to calculate Δ and Ψ. Therefore, angles outside of this range must be converted to a corresponding angle between 0° and 180°. From two sets of P and A values between 0° and 180°, the smaller pair correspond to P_2 and A_2 and the larger pair correspond to P_4 and A_4. Repeat this process for C = - 45° to obtain P and A values for zone 1 and zone 3. The ideal relationship between P and A in each zone are summarised in Equations 2-5, where subscripts refer to zone numbers.

$$P_3 = P_1 + \pi/2 \quad (2) \qquad P_4 = P_2 + \pi/2 \quad (3)$$

$$A_3 = \pi - A_1 \quad (4) \qquad A_4 = \pi - A_2 \quad (5)$$

The values of P, C and A in Figure 4 are not always the same as values read directly off the scale of the rotation mounts. To ensure the rotation mounts are reading P, C and A directly, set the fast axis of the components and the 0° scale reading on the rotation scale to lie in the plane of incidence. Check the scale reading of the rotation mounts increases as it is rotated anti-clockwise.

2.3 Calculating Phase Delay

With P and A between 0° and 180° for each zone, Δ and Ψ are calculated from Equations 6 and 7, respectively, which are derived from the average of Δ and Ψ values across the zones in Table 1. A 180° phase shift is seen upon reflection of light incident on a material with a higher refractive index than it was travelling in. Subtracting 180° from Equation 6 will remove this effect.

$$\Delta = \frac{1}{2}(P_1 + P_3 - P_2 - P_4) \tag{6}$$

$$\Psi = \frac{1}{4}(A_1 + A_2 - A_3 - A_4) \tag{7}$$

3 Theoretical Model

3.1 Jones Matrix Representation

Theoretically simulating the nulling scheme, described in Section 2, is discussed below. The behaviour of the PCSA arrangement of the null ellipsometer is described by the Jones matrices and vectors, shown in Equation 8, where P, C and A, are the angles shown in Figure 4.

$$\begin{bmatrix} X \\ Y \end{bmatrix} = \begin{bmatrix} 1 & 0 \\ 0 & 0 \end{bmatrix} \begin{bmatrix} cos(A) & sin(A) \\ -sin(A) & cos(A) \end{bmatrix} \begin{bmatrix} \rho & 0 \\ 0 & 1 \end{bmatrix}$$
$$\begin{bmatrix} cos(C) & -sin(C) \\ sin(C) & cos(C) \end{bmatrix} \begin{bmatrix} 1 & 0 \\ 0 & \pm i \end{bmatrix} \begin{bmatrix} cos(P-C) \\ -sin(P-C) \end{bmatrix} \tag{8}$$

Working backwards through Equation 8, the column vector on the right hand side represents linearly polarised

light produced by the polariser, rotated into the reference frame of the compensator. The next two matrices represent the compensator (a QWP) and a rotation matrix to move back to the reference frame of the polariser. The next matrix is the diagonal Jones matrix of the test sample where ρ is given by Equation 1. The last two matrices represent the rotation of the coordinate system into the reference frame of the analyser and the effect of the analyser (a linear polariser). Finally, the column vector on the left hand side of the equation represents the polarisation state of the beam at the detector. At the null condition, X and Y, are both zero.

3.2 Validating the Model

If r_s, r_p, δ_s and δ_p are known, they can be used at the null condition to validate Equation 8. By looping over P and A to find values corresponding to the smallest magnitude output, Equations 6 and 7 can be used to calculate Δ and Ψ. Equation 1 can also be used to determine theoretical Δ and Ψ values. If the model is correct, values from both methods will match.

The validity of the model is also confirmed by replacing the Jones matrix of the sample with an identity matrix to represent a piece of uncoated fused silica, a material known to have zero phase delay, and ensuring a zero phase delay output of the model. The model was further tested by replacing the Jones matrix of the sample with the Jones matrix of a QWP and a HWP to ensure the calculated phase delay was $\pi/2$ and π, respectively.

4 Experimental Procedure

4.1 Optical Setup

The optical setup of the null ellipsometer, shown in Figure 5, is described below. Laser light is injected from a continuous wave, laser diode source (Sacher, TEC-500-1060-030), tuneable between 1020 nm and 1080 nm, via a multi-mode optical fibre and fibre collimator to create a collimated beam with a 7 mm diameter. To ensure results are not dependent on polarisation characteristics of the laser source or launch optics, a linear cube polariser (Thorlabs, PBS103) is used to convert any variations in polarisation state of the beam to power fluctuations. Power fluctuations are later compensated for with the use of an uncoated wedge.

A QWP (Thorlabs, WPQ10M-1030) is used to create circularly polarised light to ensure a false null is not observed as the beam propagates through the system. To set the QWP to produce circularly polarised light, place the QWP, a linear polariser and detector in series after the laser source. Continuously rotate the polariser to observe a periodic pattern on the detector. Adjustment of the QWP angle will cause the amplitude of the peaks to change. Rotate the QWP until the amplitude of the peaks are minimised to achieve circular polarisation after the QWP.

Next, an uncoated wedge is used to redirect a small fraction of light to a silicon photodetector (PD1) (Gentec, PH100-Si-HA-D0) with a long pass filter (Thorlabs, FGL850M). The reading on PD1 and a second identical photodetector (PD2) at the output are used to continuously account for, and eliminate, power fluctuations of the laser source [19]. The stabilised power, P, used to determine the position of the null condition is given by Equation 9.

$$P = \frac{PD2}{PD1} \tag{9}$$

The beam then passes through the polariser, a linear plate polariser (Thorlabs, LPNIR100-MP2) with an extinction ratio of 1:100000, which turns the circularly polarised beam into a linearly polarised beam. This linearly polarised beam passes through the compensator, a QWP (Thorlabs, WPQ10M-1030), which introduces a slight ellipticity to the beam with a magnitude, such that, upon reflection off the test sample, light becomes linearly polarised. Here, the beam is linearly polarised at 90° to the angle of the analyser, a second identical linear plate polariser, where a minimum signal, or null, is observed on PD2. The test sample is mounted on a rotating breadboard and the analyser and PD2, or detection optics, are mounted on an independently rotating rail for sample measurements over a range of angles.

4.2 Optical Alignment

The null ellipsometer is aligned such that, after the wedge, the components, and the lines of holes on the rotating breadboard, lie directly along lines of holes on the optical table. Procedures in the following sections ensure accurate optical alignment of the null ellipsometer.

4.2.1 Crossed polariser alignment

To ensure the polariser and analyser are correctly positioned in their mounts, place the polariser, analyser and a photodetector in series after the laser source, without any test sample. Set the transmission axis of the polariser to be coincident with the plane of incidence, adjust the analyser until minimum transmission is observed on the photodetector, this will occur at 90°. Fix the relative positions of the polariser and analyser by rotating the scales of the rotation mounts.

4.2.2 Rotating breadboard alignment

To ensure the breadboard is aligned to the holes on the optical table, align two beams, simultaneously, to lines of holes on the optical table, shown by the solid red line in Figure 6. Install four adjustable irises (Thorlabs, IDA20), two on the line of holes on the breadboard at 0°

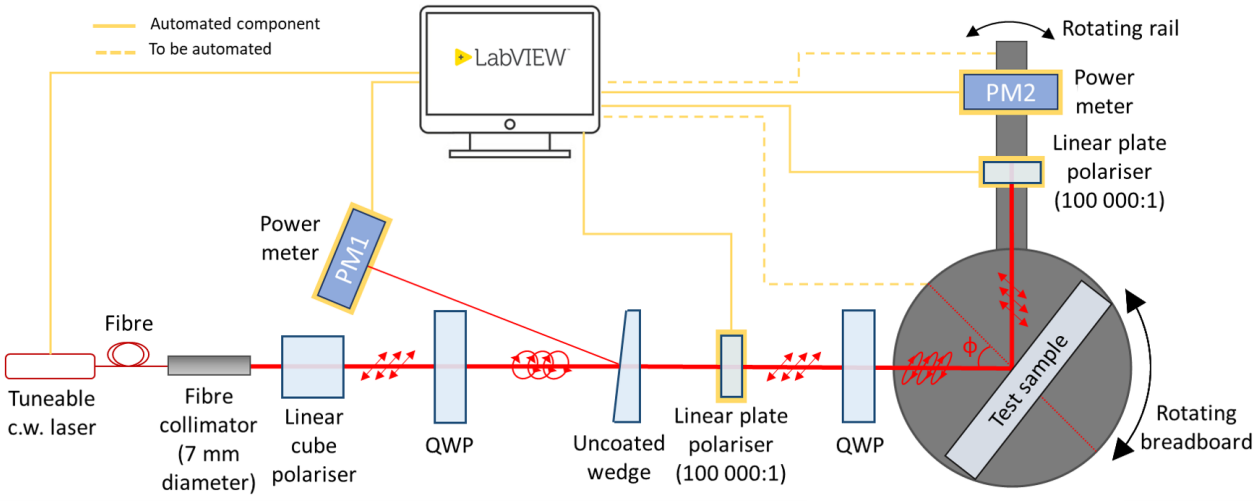

Figure 5: Experimental setup of the partially automated null ellipsometer for characterising phase delay introduced by the coating of the test sample over a range of angles.

and another two on the line of holes at 90°. When the beams are aligned to the centre of all the irises at the same time, the breadboard is aligned within an error, x°, which is quantified in Section 6.1.1.

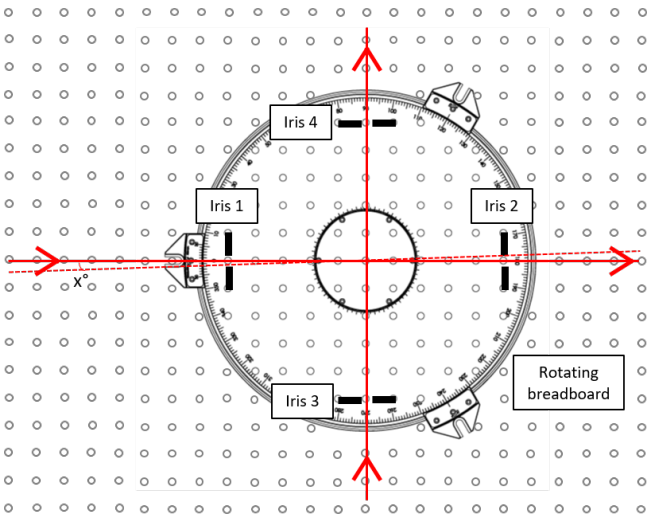

Figure 6: Experimental setup to align the breadboard within an error of ± x°. Solid red line indicates a perfectly aligned beam, dotted red line shows the largest possible misalignment, x°, in this case.

4.2.3 Sample positioning alignment

To ensure the front face of the sample sits directly above the centre of the rotating breadboard, mount the sample at 45° and mount two adjustable irises (Thorlabs, IDA25) along the line of holes on the optical table, as in Figure 7. Ensure the distance between the irises is maximised to minimise the error. By moving the sample mount, and using the fine adjusters, align the sample such that the beam passes through both irises while at their minimum aperture size of 1 mm ± 0.13 mm. The error, δ°, on the sample positioning is quantified in Section 6.1.2.

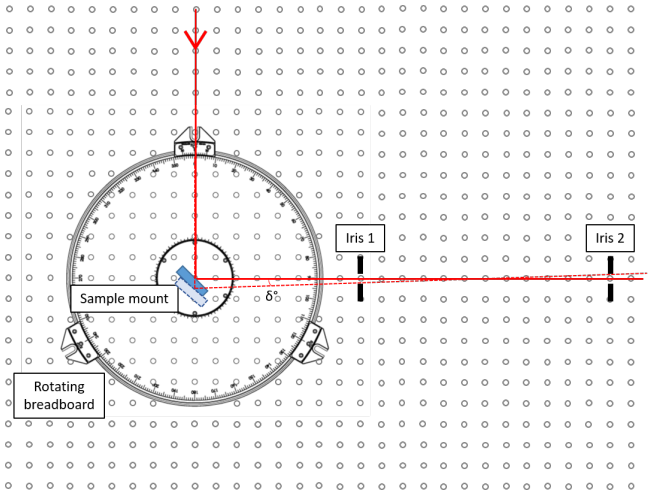

Figure 7: Experimental setup for aligning the sample mount within an error of δ°. Solid red line shows a perfectly aligned beam, dotted red line shows the largest possible misalignment in this case.

5 Control Software

The partially automated setup in Figure 5 shows automated components highlighted in yellow. Both polariser and analyser are mounted on automated rotation mounts (Standa, 8MR151-1-MEn1) and connected to LabVIEW with PD1 and PD2 where real-time power data is used to move the automated rotation mounts to angles where a minimum signal is incident on the detector. For an an-

gle of incidence, the code replicates the nulling scheme, described in Section 2.2, to find P and A in two zones, determined by the compensator setting. The logic behind the code is shown in Figure 8.

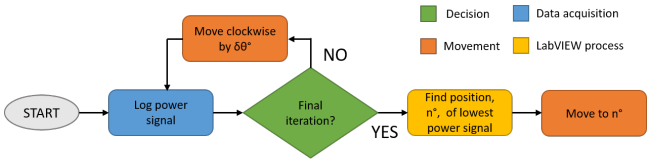

Figure 8: Flow chart displaying the logic behind the LabVIEW code where $\delta\theta°$ is the iteration step size and n° is the angle corresponding to the null position.

Initially, the polariser and analyser are set to 0°. First, the code rotates the polariser over a specified range, $\theta°$, in steps of $\delta\theta°$, saving power data at each step. At the end of the range, the code finds the position of the minimum signal, n°, and moves the polariser to this position. This process is repeated for the analyser before reducing the range and step size to converge on the null. The range and step size chosen for each iteration are summarised in Table 2. Various tests on different samples at a range of angles were used to select these values. This automated method allows for the minimum to be found to a higher degree of accuracy than through manual measurements. Residual sources of error are discussed in Section 6.2.2. Automation of the rotating breadboard, detection rail and wavelength of the tuneable laser are currently underway.

Range, $\theta°$	180	90	40	16	8	4	2
Step size, $\delta\theta°$	10	5	2	1	0.2	0.1	0.05

Table 2: Step size and ranges for code iterations.

6 Error Calculation and Calibration

6.1 Sample Angle Error

Sample angle error arises from two elements of the setup: the rotating breadboard and the sample mount positioning. Total error on the sample positioning (± 0.340°) is determined by the sum of these two errors, which are discussed in the sections below. This error is within an acceptable range, since the angle of acceptance of the photodetector is ± 0.95°. There is also a maximum error on the positioning of the breadboard of 2.13 mm, however, this does not affect the angle error and the active area of the photodetector is 10 mm. Therefore, this error is small enough for the beam to pass through the 1" optics and still be incident on the photodetector active area.

6.1.1 Rotating breadboard error

The maximum breadboard error, x°, arises from both the scale precision (± 0.0833°) (this error will reduce to 0.01° with the automated breadboard) and the error on the alignment of the breadboard to the optical table (± 0.183°). The second part is calculated using simple trigonometry, from the largest angle of sample misalignment (red dotted line in Figure 6).

Methods to reduce this error include minimising the iris aperture and maximising the distance between the two irises used for alignment. In this case, the distance between the irises was limited by the the size of the breadboard, however, a rail could be used to further extend this if necessary. Additionally, since the beam diameter is larger than the diameter of the minimum aperture of the irises, the error can be reduced with the use of a power meter to maximise the power passing through both irises, ensuring that the beam is centered.

6.1.2 Sample positioning error

Assuming the breadboard is perfectly aligned to the optical table, the maximum sample positioning error, $\delta°$, is also calculated (± 0.074°) using simple trigonometry (red dotted line in Figure 7). Additionally, the test samples are large (175 mm x 125 mm) high-reflectance mirrors, used in DiPOLE systems, which are mounted in bespoke, adjustable rectangular mounts, shown in Figure 9. To align the rectangular mounts accurately to the centre of the breadboard, a tailor-made, 3D-printed collar was designed such that, when affixed to certain holes on the breadboard, the mount sits with the front face of the optic directly above the axis of rotation of the breadboard. To ensure measurements on standard sized optics are comparable with measurements on large rectangular mirrors, bespoke adapters were made. The adapters hold 2" (Figure 9a) and 1" (Figure 9b) diameter optics with their front face over the centre of rotation of the breadboard, like the large mirrors, so calculated errors are valid for all measurements.

6.2 Phase Delay Errors

The total error on the phase delay value (± 0.240) arises from a combination of polariser, compensator and analyser errors as well as error due to the code, discussed in the sections below.

6.2.1 Polariser, compensator and analyser errors

A method for calibrating a null ellipsometer, and calculating errors on individual polariser, compensator and analyser rotation mounts is presented in the literature [20]. The standard null ellipsometer setup (Figure 5) is used to take measurements on uncoated fused silica, a material with zero phase delay, over a range of angles:

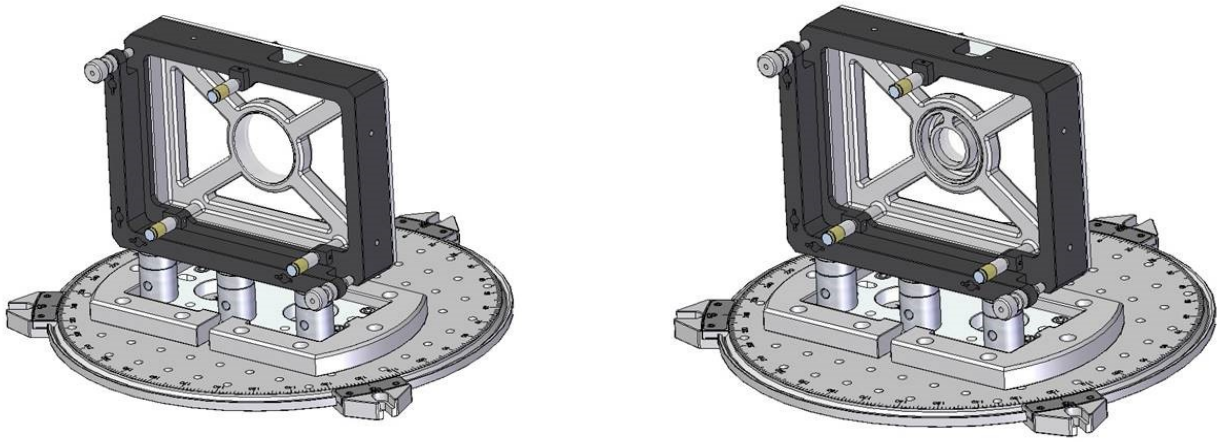

(a) (b)

Figure 9: Bespoke mirror mount adapter, for (a) 2" samples and (b) 1" samples, that sits in place of, and holds the front face of the optic in the same plane as, the 175 mm x 125 mm large high reflectance mirror. The collar around the base of the mount ensures the front face of the optics sits over the centre of rotation of the breadboard.

40°, 45°, 50°, 60°, 65° and 70°. (A measurement was not taken at 55° as the Brewster angle of fused silica is 55.409°. Measurements near the Brewster angle cause the positioning of the null to be less accurate as reflection is reduced, resulting in low powers and poor signal-to-noise ratio.) Three repeat measurements are taken for each angle and the sample position is reset each time to account for repositioning error. According to [20], resulting data forms a straight line given by Equation 10, where ResA$^-$ is given by Equation 11.

$$\langle ResA^- \rangle_{av} = 2sin(2\Psi)cos(\Delta)\delta C_c - 2\delta A_c \tag{10}$$

$$ResA^- = A_1 + A_3 - 180° \tag{11}$$

Calibration error on the compensator, δC_c, is calculated from the gradient and calibration error on the analyser, δA_c, is calculated from the intercept of the straight line. The calibration error on the polariser, δP_c, can then be calculated from Equation 12, where Res1P is the four-zone residual, given in Equation 13.

$$2\delta P_c - 2\delta C_c = -\frac{1}{2} Res1P \tag{12}$$

$$Res1P = P_1 + P_2 + P_3 + P_4 - 360° \tag{13}$$

Before the ellipsometer was automated, fully manual measurements were taken. A plot of this straight line for these manual measurements is shown in Figure 10. Errors on the polariser, compensator and analyser, from the method described above, were found to be 0.8°, 1.1° and 1.2°, respectively.

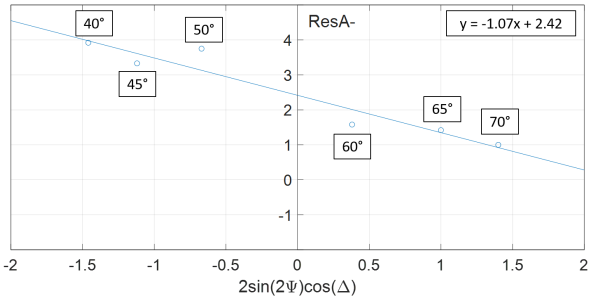

Figure 10: Plot according to [20], for manual measurements measurements with the null ellipsometer on uncoated fused-silica, used to calculate errors on the polariser, compensator and analyser. The straight line fit has a gradient value of -1.07 and intercept value of 2.42.

Repeating this procedure with the partially automated null ellipsometer (Figure 11) resulted in reduced errors on the polariser, compensator and analyser which were found to be 0.3°, 0.1° and 0.6°, respectively.

6.2.2 Error from automation

While ellipsometer automation improves overall accuracy of measurements, a small error is introduced from the automated components due to backlash. To quantify this error, the LabVIEW code for operating, and obtaining data from, the null ellipsometer was ran multiple times, without any physical adjustments to the system, to extract the error introduced solely by the code (± 0.05°).

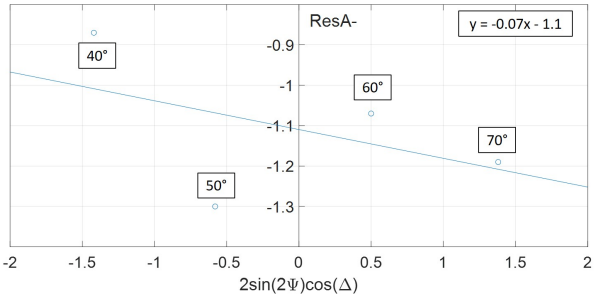

Figure 11: Plot according to [20], for automated measurements measurements with the null ellipsometer on uncoated fused-silica, used to calculate errors on the polariser, compensator and analyser. The straight line fit has a gradient value of -0.07 and intercept value of -1.10.

6.3 Reducing Phase Delay Errors

Due to the nature of the experimental procedure, the signal-to-noise ratio observed in the vicinity of the null is much lower than at other polariser and analyser positions. One method of improving the signal to noise ratio at the null condition is by increasing the laser power, however, this is limited by the damage threshold of the photodetector. A potential solution is to start with a given laser power and to increase the power when in the vicinity of the null, however, this has not yet been implemented due to technical complexity. Another method to reduce the signal-to-noise-ratio is to remove as much background light as possible. Therefore, the setup is fully enclosed to isolate the results from changes in the background conditions.

A technique for reducing null positioning errors, without changing the power of the laser source, is called the method of swings. This method relies on the fact that the signal on the detector is a parabolic function of the polariser and analyser angles, about the null. The polariser, or analyser, angle for equal signals either side of the null are recorded and the angle position in the middle of these two corresponds to the true position of the null. This method can improve the precision of the null ellipsometer ten-fold [21], however, it has not yet been employed here.

Alternative methods in the literature for improving the performance of a null ellipsometer include: motor-driven, self-nulled ellipsometers with modulators [22] and self-nulled ellipsometers, with no moving parts, that employ Faraday cells [23].

7 Results

The null ellipsometer was used to measure the phase delay introduced by a large-aperture, high-reflectance coating used in the DiPOLE multi-pass. The operational angle, or the angle for which the reflectance is optimised, is 45.0°. Mirror characteristics, such as reflectance, scatter and damage resilience, are optimised at these angles; however, as shown by Figure 3, it is predicted that phase delay is not zero at the operational angle.

Figure 12 shows both theoretical (orange solid line) and experimental (blue dotted line) phase delay values for the 45° high-reflectance coating for angles of incidence between 40° and 60°. Experimental measurements indicate a phase delay value of 21.0° at the operational angle and zero phase delay at an angle of incidence of 54.3°. Theoretical values indicate a phase delay of 1.5° at the operational angle and zero phase delay at an angle of incidence of 45.7°.

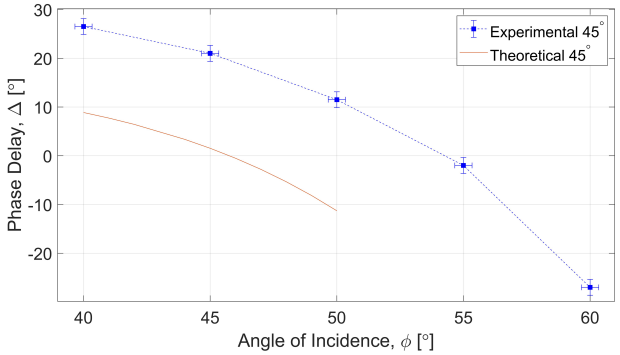

Figure 12: Phase delay results for a 45.0° mirror comparing experimental measurements on a standard coating and an optimised coating with theoretical values.

8 Discussion

Figure 12 highlights a discrepancy between the theoretical and experimental phase profiles. The main source of this error arises from spectrophotometric measurements used to spectrally position the coatings. Although measurements at the time of production indicated that the spectral position was correct, experimental values are larger than theoretical values, therefore, the deposited coating is likely thicker than the design. In addition, environmental factors, such as moisture trapped in the coating, can cause the spectral positioning to drift by 2-3 nm, meaning the coating is no longer optimised for the operational wavelength of 1030 nm.

Despite the discrepancy, the theoretical phase profile used to design the deposited coating does not predict a phase delay of zero at the operational angle. Therefore, if Manx Precision Optics can produce a coating with a lower theoretical phase delay, the experimental phase delay is expected to be lower.

9 Conclusion and Future Work

To summarise, an automated null ellipsometer was designed and developed to accurately characterise the

phase delay introduced by high-reflectance mirror coatings. A discrepancy between theoretical and experimental values was found. This has allowed Manx Precision Optics to produce a new batch of mirror coatings with a lower theoretical phase delay.

Future work includes characterising the phase delay values of these new mirror coatings as well as measuring reflectance, scatter and damage resilience to ensure these properties have not been compromised in the endeavour for zero phase delay. To better understand the coating process, other tests include testing the large-aperture mirror coatings at different points across the coating as well as comparing two mirrors from the same coating run to see if the phase delay of the sample is affected by its position in the coating chamber.

References

[1] R. Sundar, P. Ganesh, R. Kishor Gupta, G. Ragvendra, B. K. Pant, V. Kain, K. Ranganathan, R. Kaul and K. S. Bindra.*Laser Shock Peening and its Applications: A Review*, Lasers Manuf. Mater. Process, 6, 424-463 (2019).

[2] R. Betti and O. A. Hurricane. *Inertial-confinement fusion with lasers*, Nature Physics, 12, 435-448 (2016).

[3] U. Zastrau, M. McMahon, K. Appel, C. Baehtz, E. Brambrink, R. Briggs, T. Butcher, B. Cauble, B. Chen, H. Damker, C. Deiter, J. Eggert, K. Falk, L. Fletcher, S. H. Glenzer, S. Göde, M. Harmand, A. Higginbotham, Z. Konopkova, D. Kraus, H. -P. Liermann, M. Nakatsutsumi, A. Pelka, G. Priebe, R. Redmer, A. Schropp, R. Smith, P. Sperling, I. Thorpe and S. Toleikis. *Conceptual Design Report: Dynamic Laser Compression Experiments at the HED Instrument of European XFEL*, XFEL.EU TR-2017-001 (2017).

[4] P. Mason, M. Divoky, K. Ertel, J. Pilar, T. Butcher, M. Hanus, S. Banerjee, J. Phillips, J. Smith, M. De Vido, A. Lucianetti, C. Hernandez-Gomez, C. Edwards, T. Mocek and J. Collier. *Kilowatt average power 100 J-level diode pumper solid state laser*, Optica, 4(4), 438-439 (2017).

[5] S. Banerjee, P. Mason, J. Phillips, J. Smith, T. Butcher, J. Spear, M. De Vido, G. Quinn, D. Clarke, K. Ertel, C. Hernandez-Gomez, C. Edwards and J. Collier. *Pushing the boundaries of diode-pumped solid-state lasers for high-energy applications*, HPL Letters, 9 (2020).

[6] M. Divoký, J. Pilař, M. Hanuš, P. Navrátil, O. Denk, P. Severová, P. Mason, T. Butcher, S. Banerjee, M. De Vido, C. Edwards, J. Collier, M. Smrž, and T. Mocek. *150 J DPSSL operating at 1.5 kW level*, Opt. Lett., 46, 5771-5773 (2021).

[7] M. De Vido. *DiPOLE 100Hz*, `https://www.clf.stfc.ac.uk/Pages/DiPOLE-100Hz.aspx`

[8] J. P. Phillips, S. Banerjee, P. Mason, J. Smith, J. Spear, M. De Vido, K. Ertel, T. Butcher, G. Quinn, D. Clarke, C. Edwards, C. Hernandez-Gomez and J. L. Collier. *Second and third harmonic conversion of a kW average power, 100 J-level diode pumped Yb:YAG laser in large aperture LBO*, Optics Letters, 46(8), 1808-1811 (2021).

[9] M. Aoyama, K. Yamakawa, Y. Akahane, J. Ma, N. Inoue, H. Ueda and H. Kiriyama. *0.85-PW, 33-fs Ti:sapphire laser*, Optics Lett., 28(17), 1594-1596 (2003).

[10] W. P. Leemans, J. Daniels, A. Deshmukh, A. J. Gonsalves, A. Magana, H. S. Mao, D. E. Mittelberger, K. Nakamura, J. R. Riley, D. Syversrud, C. Toth and N. Ybarrolaza. *Bella Laser and Operations*, Proceedings of PAC2013, Pasadena, CA USA (2013).

[11] D. N. Papadopoulos, J. P. Zou, C. Le Blanc, L. Ranc, F. Druon, L. Martin, A. Fréneaux, A. Beluze, N. Lebas, M. Chabanis, C. Bonnin, J. B. Accary, B. L. Garrec, F. Mathieu and P. Audebert. *First commissioning results of the Apollon laser on the 1 PW beam line*, in Conference on Lasers and Electro-Optics, OSA Technical Digest (Optical Society of America, 2019), paper STu3E.4. (2019).

[12] R. Allott, S. Astbury, S. Banerjee, B. Bingham, S. Blake, N. Booth, N. Bourgeois, C. Brenner, P. Brummit, E. Bryce, A. Boyle, T. Butcher, D. Carroll, O. Chekhlov, R. Clarke, J. Collier, J. Dymoke-Bradshaw, K. Ertel, C. Edwards, M. Galimberti, C. Gregory, J. Green, M. Harman, S. Hawkes, R. Heathcote, C. Hernandez-Gomez, S. Hook, C. Hooker, A. Lintern, V. Marshall, P. Mason, I. Musgrave, D. Neely, P. Norreys, R. Pattathil, J. Phillips, A. Robinson, D. Rusby, G. Scott, R. Scott, C. Spindloe, M. Stefania, B. Summers, D. Symes, Y. Tang, R. Taylor, S. Tomlinson, D. Treverrow, R. Trines, M. Tyldesley, M. De Vido, G. Wiggins, L. Wilson, A. Wyatt, B. Wyborn et al. *PULSAR Technical Design Report*, Central Laser Facility, Science and Technology Facilities Council, Rutherford Appleton Laboratory (2016).

[13] J. Pilar, M. De Vido , M. Divoky, P. Mason, M. Hanusa, K. Ertel, P. Navratila, T. Butcher, O. Slezaka, S. Banerjee, J. Phillips, J. Smith, A. Lucianetti, C. Hernandez-Gomez, C. Edwards, J. Collier and T. Mocek. *Characterization of "Bivoj / DiPOLE 100" – HiLASE 100 J / 10 Hz diode pumped solid state laser*, Proc. SPIE, 10511, 1-7 (2018).

[14] W. C. Scott and M. De Wit. *Birefringence compensation and TEM00 mode enhancement.* Appl. Phys. Lett., 18(3), 3-4(1971).

[15] J. Richards/ *Birefringence compensation in polarisation coupled lasers*, Appl. Opt., 26(13), 2514-7 (1987).

[16] H. G. Tompkins and E. A. Irene. *Handbook of Ellipsometry*, Springer, 10th Edition (2005).

[17] F. L. McCrackin, E. Passaglia, R. R. Stromberg, and H. L. Steinberg. *Measurement of the Thickness and Refractive Index of Very Thin Films and the Optical Properties of Surfaces by Ellipsometry*, J Res Natl Bur Stand A Phys Chem., 67A(4), 372-376 (1963).

[18] P. Nestler and C. A. Helm. *Determination of refractive index and layer thickness of nm-thin films via ellipsometry*, Optics Express, 25(22), 27077-27085 (2017).

[19] C. Chatwin and I. A. Watson. *Efficient laser power and energy monitoring using an uncoated wedge*, Applied Optics, 28(2), 209-21 (1989).

[20] R. M. A. Azzam and N. M. Bashara. *Calibration, of Ellipsometer Divided Circles*, J. Opt. Soc. Am., 61, 1118 (1971).

[21] R. M. A. Azzam and N. M. Bashara. *Ellipsometry and Polarised Light*, 403. North-Holland (1977).

[22] H. Takasaki. *Automatic Ellipsometer. Automatic Polarimetry by Means of an ADP Polarization Modulator III*, Appl. Opt., 5(5), 759-764 (1966).

[23] H. J. Mathieu, D. E. McClure and R. H. Muller. *Fast self-compensating ellipsometer*, Review of Scientific Instruments, 45(6), 789-802 (1974).